International Journal of Heat and Fluid Flow 29 (2008) 1060–1070

Contents lists available at ScienceDirect

International Journal of Heat and Fluid Flow

journal homepage: www.elsevier.com/locate/ijhff

# Numerical study of the near wake of a circular cylinder

J.G. Wissink *, W. Rodi

*Institute for Hydromechanics, University of Karlsruhe, P.O. Box 6980, D-76128 Karlsruhe, Germany*

ARTICLE INFO

*Article history:*
Received 2 August 2007
Accepted 1 April 2008
Available online 21 May 2008

*Keywords:*
DNS
Wake
Vortices
Turbulence

ABSTRACT

A series of direct numerical simulations (DNS) of incompressible flow around a circular cylinder at $Re = 3300$ – based on the far field velocity and the diameter of the cylinder $D$ – were performed. After taking an offset in the streamwise direction into account, the results were found to be in good agreement with experimental data obtained at a slightly higher Reynolds number of $Re = 3900$. Increasing the spanwise size of the computational domain from $l_z = 4D$–$8D$ was found to only marginally affect the profiles of turbulence statistics in the wake of the cylinder, although even in the simulation with $l_z = 8D$ the spanwise autocorrelation of $u$ did not completely converge to zero towards the sides of the computational domain. The phase-averaged statistics showed the existence of shear layers immediately downstream of the cylinder, which originated from the boundary layers along the top and bottom surface of the cylinder. As the shear layers rolled-up, significant production of turbulence kinetic energy was observed inside the rolls of recirculating flow. At $x/D = 6$ snapshots of the flow field were gathered. At this location, individual vortices – shed from the upper and lower shear layer, respectively, behind the cylinder – could still be identified. The gathered wake data will be used to study the influence of large meandering coherent structures on the promotion of laminar heat transfer along a body located downstream of the cylinder.



## 1. Introduction

The flow past circular and square cylinders comprises a rich variety of different phenomena and has been a popular testing ground for various numerical simulation methods. With increasing Reynolds number, the dynamics of the flow around a circular cylinder changes significantly: for very small Reynolds numbers the wake consists of a steady recirculation region behind the cylinder. Though Monkewitz (1988) showed the existence of a local absolute instability in the wake at a Reynolds number of $Re = 25$, a von Karman vortex street was first found to appear at a Reynolds number somewhere around 49 (see Williamson, 1996b). At a critical Reynolds number of $Re_{crit} \approx 194$ the wake flow becomes three-dimensional. The first three-dimensional instability that appears is the so-called "mode A instability" that is characterized by a spanwise wave-length of around $3D - 4D$, where $D$ is the diameter of the cylinder. This mode is the result of an elliptic instability and it scales on the primary vortex core, which is the larger physical structure in the flow. Around $Re \approx 240$ the instability changes from mode A to mode B. Mode B is characterized by a reduction in size of the spanwise wave-length by a factor of three. This instability scales on the braid shear layer which is the smaller physical structure of the flow (see also Williamson, 1996a and Thompson et al., 1996). In the subcritical range – for Reynolds numbers between $Re = 1000$ and $Re = 200{,}000$ – the flow in the vicinity of the cylinder is entirely laminar and transition happens somewhere in the free shear layer downstream of the cylinder. With increasing Reynolds number, the location of transition gradually moves upstream. For Reynolds numbers beyond $Re = 200{,}000$, the location of transition has moved so far upstream that the boundary layer along the cylinder becomes partially turbulent. As a consequence, the boundary layer separation downstream is deferred thereby reducing the size of the wake and, because of that, also the losses.

At $Re = 3900$, in the lower subcritical range, several experiments – such as the ones by Lourenco and Shih (1993), Norberg (1994), Ong and Wallace (1996) and Dong et al. (2006) – were carried out (a detailed review of experiments is provided in Norberg, 2003). It has become a popular test case for numerical methods. Though also some Direct Numerical Simulations (DNS) – see for instance Ma et al. (2000) and Dong et al. (2006) – were carried out, most of the publications were concerned with Large Eddy Simulations (LES) (such as the ones performed by Beaudan and Moin, 1994; Mittal and Moin, 1997; Breuer, 1998; Fröhlich et al., 1998 and Kravchenko and Moin, 2000).

One of the important issues that needs to be addressed is the influence of the spanwise size of the computational domain on the turbulence statistics in the near wake. Ma et al. (2000)

* Corresponding author. Present address: School of Engineering and Design, Brunel University, Uxbridge, Middlesex UB8 3PH, UK. Tel.: +44 1895 267371; fax: +44 1895 256392.
*E-mail address:* jan.wissink@brunel.ac.uk (J.G. Wissink).

0142-727X/$ - see front matter © 2008 Elsevier Inc. All rights reserved.
doi:10.1016/j.ijheatfluidflow.2008.04.001

performed a detailed study and observed two states in the near wake. The first state was characterized by the presence of a "U-shaped" profile of the streamwise velocity, while the second state was characterized by the presence of a "V-shaped" profile. While the "U-shaped" profile appeared only in the well-resolved simulations with a spanwise size up to $l_z = \pi D$, the "V-shaped" profile appeared in both the marginally resolved simulations – with a spanwise size of $l_z = \pi D$ – and in the only well-resolved simulation with a spanwise size of $l_z = 2\pi D$. In the LES of Breuer (1998) – performed on a relatively coarse mesh – only "U-shaped" profiles were obtained for both a spanwise size of $l_z = \pi D$ and a spanwise size of $l_z = 2\pi D$. In the paper of Kravchenko and Moin (2000) it is speculated that the "V-shaped" profile is an artefact and the "U-shaped" profile – which reflects the presence of laminar free-shear layers – is more likely to persist even at larger spanwise sizes, $l_z$, than the ones $l_z \leqslant \pi D$ used in their paper.

This paper reports on the results of a series of DNS of flow around a circular cylinder at $Re = 3300$. The Reynolds number was chosen in order to reproduce accurately the near wakes from the experiments of Liu and Rodi (1994a,b). In these experiments, the flow around and heat transfer from a heated turbine blade has been studied in the presence of periodically incoming wakes generated by a rotating squirrel cage placed in the inflow. Based on the experiments, a set of DNS of flow and heat transfer in a linear turbine cascade with incoming wakes were performed (see Wissink and Rodi, 2006). The wakes from the experiments – generated by the downstream cylinders mounted in the squirrel cage – were substituted by artificial wake data. This artificial data was generated using a precursor LES and correspond to the far field of a turbulent wake. The increase in laminar heat transfer – as found in the experiments due to the influence of incoming wakes – could only be partially reproduced in the DNS. The observed difference in laminar heat transfer might be accounted for by a difference in the spectral contents between the artificial (far field) wakes used in the DNS and the cylinder-generated near field wakes in the experiments. To verify this, new wake data generated in the present DNS study – that was recorded in the near wake at $x/D = 6$ – will be used as input in a further DNS of flow and heat transfer in the turbine cascade studied in Wissink and Rodi (2006), whereby the influence of vortical structures from the near wake on the promotion of laminar heat transfer from the heated blade will be investigated.

In the present DNS of flow around a circular cylinder, the spanwise size of the computational domain was varied from $l_z = 4D$ to $l_z = 8D$ to allow a study of its influence on the turbulence statistics in the near wake. In addition to the time-averaged turbulence statistics, for the simulation with a large span, also phase-averaged turbulence statistics are presented using the mean shedding period as a base. The accuracy of the results is checked by employing a grid refinement study and by performing a comparison with the experiments of Lourenco and Shih (1993) (which were carried out at a slightly higher Reynolds number of $Re = 3900$).

## 2. Numerical aspects

The simulations were performed using a finite-volume code with a collocated variable arrangement and a curvilinear mesh. In the code, a second-order accurate central discretization in space was combined with a three-stage Runge-Kutta method for the time-integration. To avoid a decoupling of the velocity field and the pressure field, the momentum interpolation technique of Rhie and Chow (1983) was employed. The Poisson equation for the pressure was iteratively solved using the SIP-solver of Stone (1968). The code was parallellized using the standard Message Passing Interface (MPI) protocol. For a more detailed description of the code see Breuer and Rodi (1996).

The computational geometry employed in all simulations is shown in Fig. 1 (left). At the inflow plane a uniform flow field with $(u, v, w)^t = (1, 0, 0)^t U_0$ was prescribed. At the top and the bottom free-slip boundary conditions were used while at the surface of the cylinder a no-slip condition was employed. At the outflow plane a convective outflow condition was used and in the spanwise direction periodic boundary conditions were employed. For all performed DNS, the employed computational mesh, the maximum size of the wall-nearest grid-cell, $\Delta\theta^+ \times \Delta r^+ \times \Delta z^+$ (in wall-units) and the spanwise size, $l_z$, of the computational domain are listed in Table 1. In Fig. 1 (right) a detail of the O-mesh in the $(x, y)$ plane employed in Simulations D and E is shown. Because of the dense grid, only every eighth grid-line is displayed. It can be seen that the grid near the cylinder is only stretched in the radial direction. This was done to avoid the occurence of numerical inaccuracies due to unfavourable cell aspect ratios. The time step employed in the simulations is $\delta t = 5 \times 10^{-4} D/U_0$.

In order to trigger both vortex shedding and the transition to turbulence, after a transient period of approximately $25D/U_0$ time-units, random disturbances were added to the instantaneous velocity field. Statistics were subsequently stored after a second transient period of at least $30D/U_0$ time-units. In Simulation E, phase-averaged statistics were gathered during 10 vortex shedding

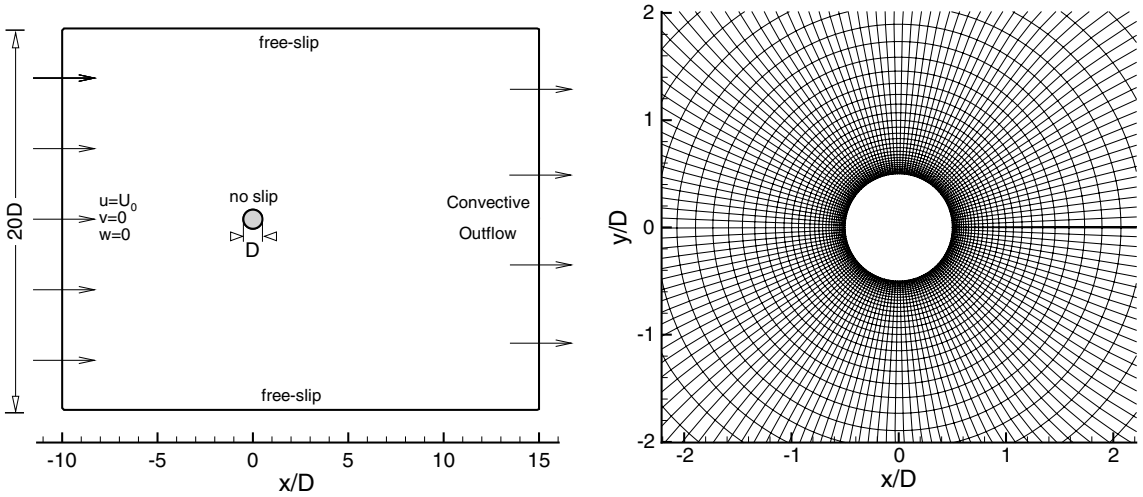


**Fig. 1.** Left: Computational geometry, Right: O-mesh in the vicinity of the cylinder showing every 8th grid-line from Simulations D and E.

**Table 1**
Overview of the DNS of flow around a circular cylinder at $Re = 3300$ – based on far field velocity and cylinder diameter

| Simulation | Grid | $\Delta\theta^+ \times \Delta r^+ \times \Delta z^+$ | $l_z$ |
|---|---|---|---|
| A | $406 \times 156 \times 256$ | $5.4 \times 1.03 \times 10.6$ | $4D$ |
| B | $606 \times 201 \times 512$ | $3.54 \times 0.68 \times 5.3$ | $4D$ |
| C | $906 \times 306 \times 512$ | $2.34 \times 0.67 \times 5.3$ | $4D$ |
| D | $1206 \times 406 \times 512$ | $1.74 \times 0.66 \times 5.3$ | $4D$ |
| E | $1206 \times 406 \times 1024$ | $1.74 \times 0.66 \times 5.3$ | $8D$ |

$\Delta\theta^+ \times \Delta r^+ \times \Delta z^+$ is the maximum size among all wall-nearest grid cells (in wall-units) – where $\theta$ is the coordinate in the circumferential direction, $r$ is the coordinate in the radial direction and $z$ is the coordinate in the spanwise direction – $l_z$ is the spanwise size of the domain and $D$ is the diameter of the cylinder.

cycles using a period of $T = 1/St$, where $St$ is the Strouhal number which is the frequency of the vortex shedding made dimensionless using the mean inflow velocity $U_0$ and the the diameter of the cylinder $D$. The period $T$ was subdivided into 64 equal phases $\phi = 0, 1/64, \ldots, 63/64$. The phase-averaging was combined with spatial averaging in the homogeneous spanwise direction.

## 3. Results

### 3.1. Study of the instantaneous flow

As the boundary layer along the upper and lower parts of the cylinder surface detaches, free-shear layers are formed. An illustration of this is given in Fig. 2, where a sequence of three snapshots with iso-surfaces of the spanwise vorticity at $\omega_z = \pm 10U_0/D$ is shown. The shear layers consisting of positive or negative vorticity can be seen to alternatively roll-up forming a vortex street as the vorticity is washed downstream. Immediately upstream of the location where the – mainly two-dimensional – free-shear layers roll-up, a spanwise modulation in the shear layers can be observed. The location of this modulation approximately corresponds to the onset of transition from a 2D to a 3D flow. To correctly reproduce the physics in the near wake, it is of paramount importance that the free-shear layers are well-resolved.

Fig. 3 illustrates the formation of the vortex street somewhat downstream of the circular cylinder using a series of three snapshots showing iso-surfaces of the fluctuating pressure $p' = p - \bar{p}$. The iso-surface identifies those areas where the fluid rotates. The snapshot at $t = 53.50D/U_0$ shows a roll of recirculating flow that originates from the shear layer from the upper surface of the cylinder. At $t = 55.00D/U_0$, the roll has been convected further downstream by the mean flow. At $t = 56.50D/U_0$, finally, the roll begins to disintegrate, illustrating the increasing three-dimensionality of the structures in the downstream direction.

### 3.2. Time-averaged statistics

Table 2 provides an overview of the Strouhal number $St$, and the location of separation of the time-averaged flow field, $\alpha$, as found in Simulations A–E. The Strouhal number was found not to be very sensitive to the resolution of the flow field, while the location of separation can be seen to move upstream slightly as the computational mesh becomes finer.

As can be seen in Fig. 4, the minimum of the $U$-velocity profile in the experiments is located $0.4D$ upstream of the minimum $U$-velocity obtained in the present DNS. The offset observed in the location of the minima is partially a consequence of the difference in Reynolds number between DNS ($Re = 3300$) and experiments ($Re = 3900$) and partially due to the possible presence of background noise in the experiments leading to early transition. As shown in the figure, a difference in magnitude and location of

**Table 2**
Strouhal number $St$ and the (time-averaged) location of separation, $\alpha$ (in degrees), where $\alpha = 0^\circ$ corresponds to the stagnation line at $(x/D, y/D) = (-\frac{1}{2}, 0)$

| Simulation | $St$ | $\alpha$ (°) |
|---|---|---|
| A | 0.216 | 90.3 |
| B | 0.221 | 88.6 |
| C | 0.216 | 87.8 |
| D | 0.214 | 87.3 |
| E | 0.216 | 87.4 |

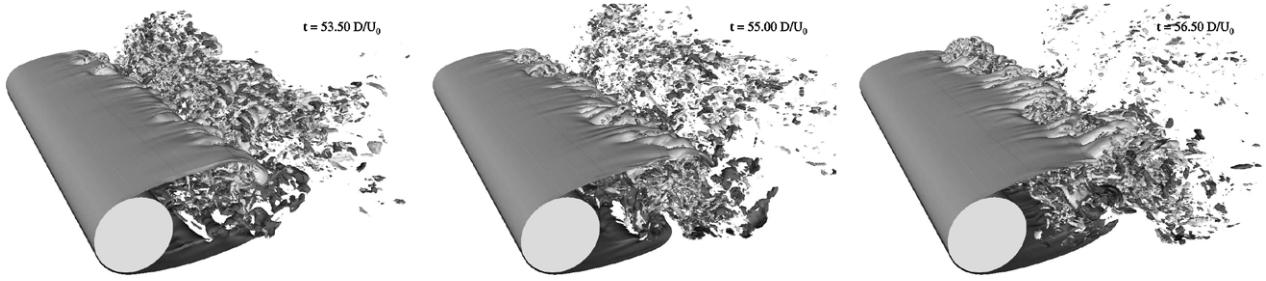


**Fig. 2.** Simulation E: a sequence of three snapshots at $t = 53.50D/U_0$, $55.00D/U_0$ and $56.50D/U_0$ of spanwise vorticity iso-surfaces at $\omega_z = 10U_0/D$ (dark surface) and $\omega_z = -10U_0/D$ (light surface).

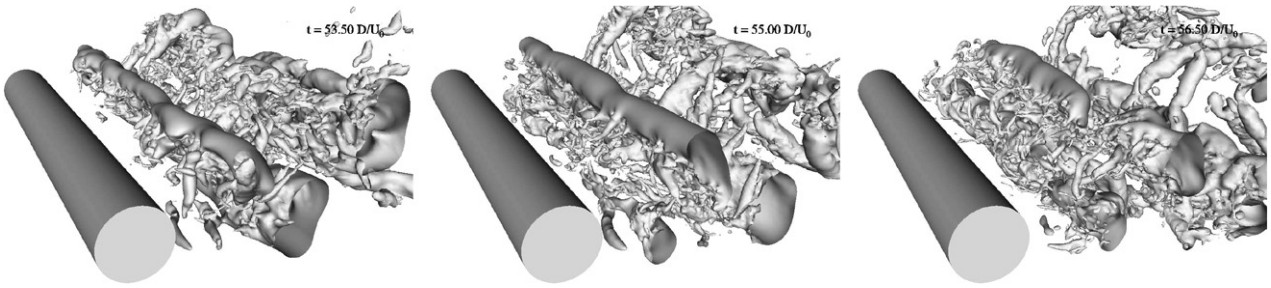


**Fig. 3.** Simulation E: A sequence of three snapshots at $t = 53.50D/U_0$, $55.00D/U_0$ and $56.50D/U_0$ of the iso-surface of the fluctuating pressure at $p' = -0.1$.

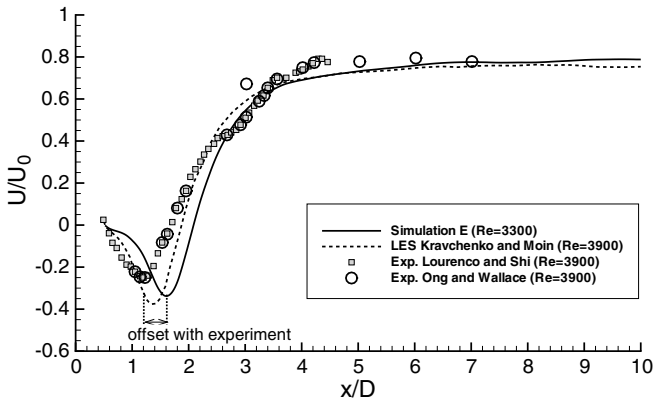


**Fig. 4.** Mean $u$-velocity for Simulation E – normalized by the mean inflow velocity $U_0$ – along the centre line ($y/D = 0$) of the computational domain, compared to the LES results of Kravchenko and Moin (data taken from Kravchenko and Moin, 2000) and the experiments of Lourenco and Shih (1993) and Ong and Wallace (1996).

the minima between numerical simulation and experiments was also observed in the LES results reported by Kravchenko and Moin (2000). Because of the slightly higher Reynolds number in the LES, compared to the DNS, the minimum is located further upstream. Kravchenko and Moin attributed the difference between their LES and the experiments to the presence of external noise in the experiments that led to a reduction in size of the recirculation region. The differences between LES and DNS are likely to be due to the difference in Reynolds number.

The quality of the DNS was assessed not only by comparison with experiment, but also by performing a series of simulations in which the number of grid points is subsequently increased. A comparison of the statistical quantities obtained in Simulations A–E is shown in Figs. 5 and 6. In Fig. 5 (upper pane) the time-averaged $u$-velocities from Simulations A–E are compared to one another at various locations in the wake. At $x/D = 1$, a "U-shaped" profile is obtained in the well-resolved simulations, while in Simulation A a "V-shaped" profile is obtained. The "U-shaped" profiles reflect the presence of two – intact, virtually two-dimensional – free shear layers at $y/D \approx \pm\frac{1}{2}$, corresponding to the two detached non-turbulent boundary layers from the top and bottom of the cylinder shown in Fig. 2 combined with a dead air region immediately behind the cylinder. In Simulation A, the ill-resolved shear layers undergo early transition thereby loosing their coherence and more fluctuations penetrate the region immediately behind the cylinder, which results in a "V-shaped" profile at $x/D = 1$. Farther downstream, at $x/D = 2$, all simulations show a "V-shaped" profile, illustrating that at this location the free-shear layers have largely been destroyed by turbulent motion. For $x/D \geqslant 3$, the mean $u$-velocity profiles obtained in Simulations C–E become very similar to one another.

Fig. 5 (lower pane) shows a comparison of the time-averaged $v$-velocity profiles from Simulations A–E at the same locations as the profiles shown in Fig. 5 (upper pane). With an increasing number of grid points, a gradual convergence to the results from Simulations D and E can be observed. At $x/D = 2$, two large peaks at $y/D \approx \pm\frac{1}{2}$ can be seen in the mean $v$-velocity profile. These peaks exactly correspond to the $y$-location of the free-shear layers upstream and indicate the presence of a vertical oscillatory motion of the shear layers which is induced by the vortex shedding.

In Fig. 6 (upper and middle pane), profiles of the normal stresses $\overline{u'u'}$ and $\overline{v'v'}$ are shown at the same locations as the profiles in Fig.

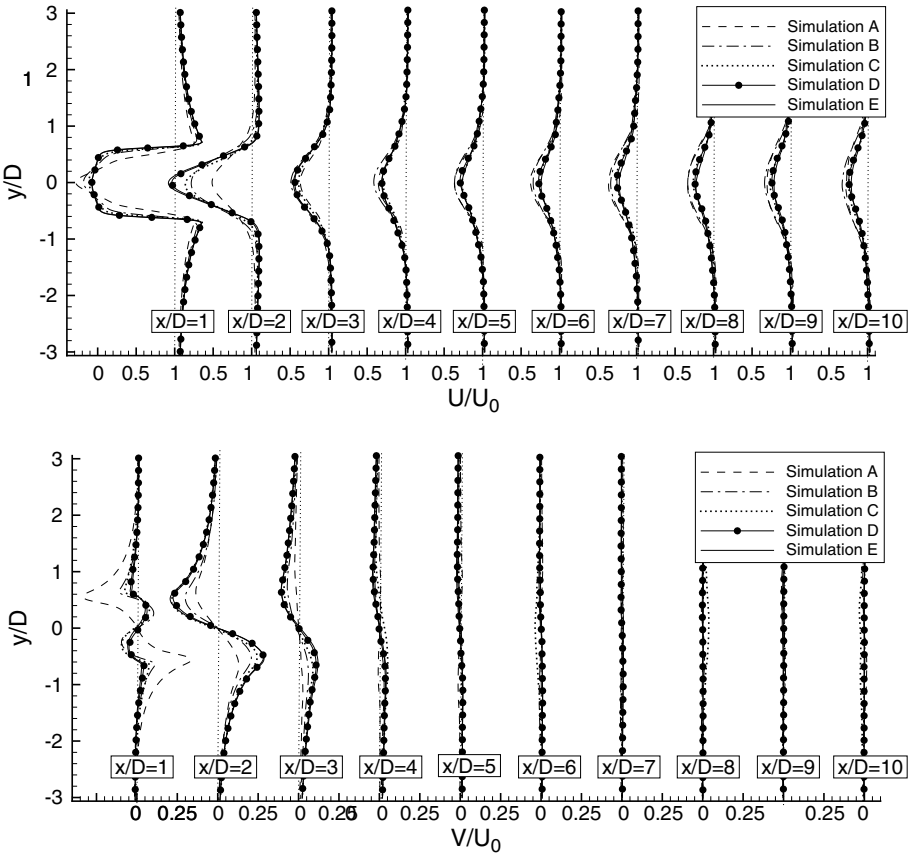


**Fig. 5.** Mean $u$-velocity profiles (above) and mean $v$-velocity profiles (below) from Simulations A–E at the locations $x/D = 1, 2, \ldots, 10$ in the wake of the circular cylinder.

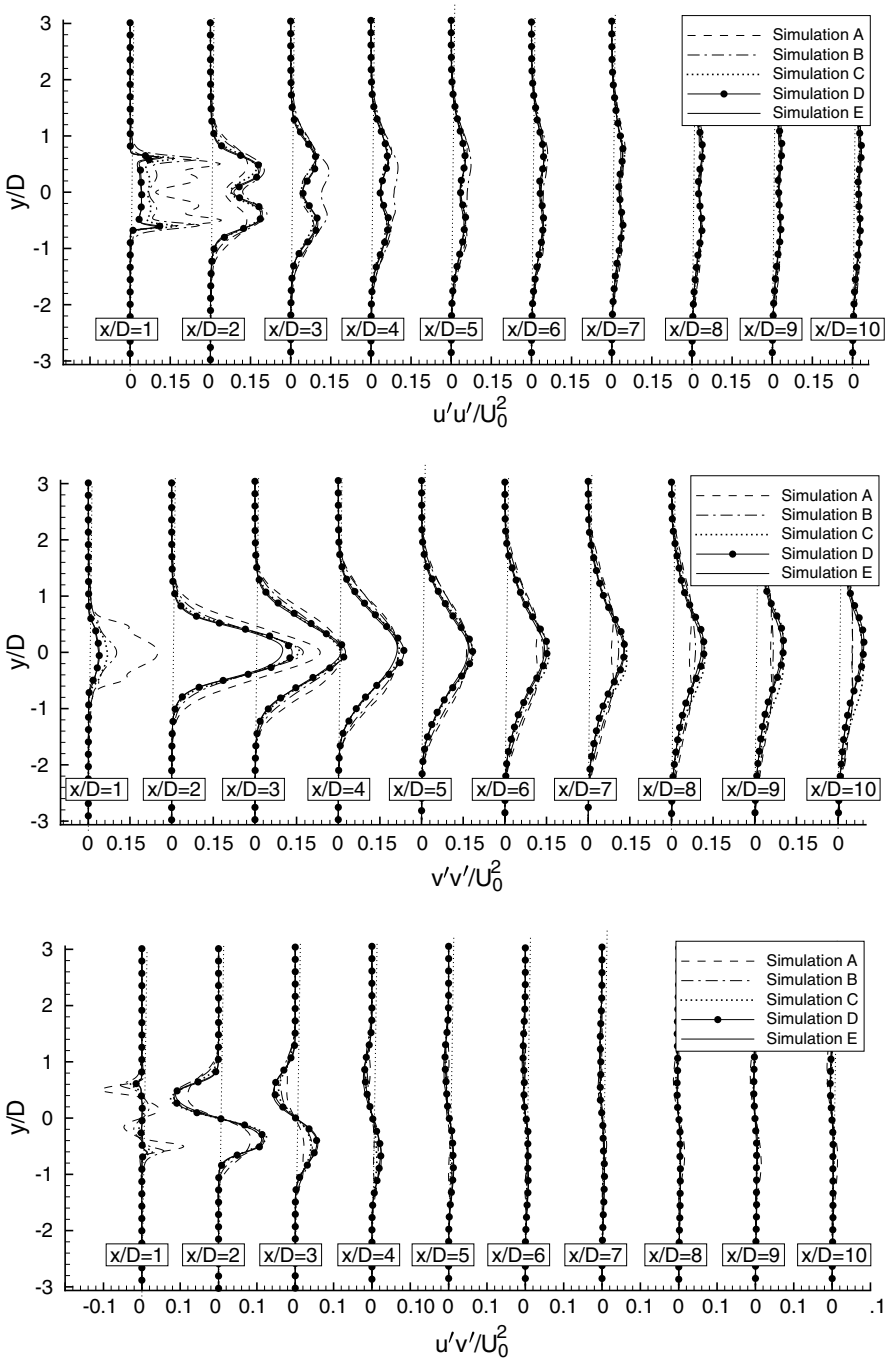


**Fig. 6.** Reynolds stress profiles for Simulations A–E at the locations $x/D = 1, 2, \ldots, 10$ in the wake of the circular cylinder. Upper pane: $\overline{u'u'}$, Middle pane: $\overline{v'v'}$, lower pane: $\overline{u'v'}$.

5. Fig. 6 (upper pane) shows that with increasing resolution the peaks in the streamwise fluctuations at $x/D = 1$ significantly reduce and become more and more localized near $y/D \approx \pm\frac{1}{2}$. Farther downstream, at $x/D = 2$, the two peaks in the well-resolved simulations are found to become significantly larger and wider, illustrating the gradual destruction of the two shear layers that starts with the roll-up of the layers followed by further transition to turbulence. For $x/D \geqslant 3$, the peaks gradually become smaller and wider at such a slow rate that they remain visible at all stations up to and including $x/D = 10$. In Fig. 6 (middle pane), the peak in the $\overline{v'v'}$-profile at $x/D = 1$ shows a gradual decline with increasing resolution, illustrating that the turbulence is not able to significantly affect the flow immediately behind the cylinder. The largest peak can be seen at $x/D = 2$. In the vicinity of this location the shear layers actually roll-up generating large vertical movements. Farther downstream the peaks gradually decline.

Fig. 6 (lower pane) shows $\overline{u'v'}$-profiles at $x/D = 1, 2, \ldots, 10$. As also observed above for the other turbulence statistics, at $x/D = 1$ the results of the marginally resolved Simulation A differ significantly from the results obtained in the other simulations. The largest peaks in the shear stress are observed at $x/D = 2$ and $y/D \approx \pm\frac{1}{2}$. Farther downstream the peaks become smaller and gradually diffuse.

In Fig. 7 (left) the mean $u$-velocity profiles of Simulations D and E are compared to the experiments of Lourenco and Shih (1993) at the locations $x/D = 1.06, 1.54, 2.02$. Taking an offset of $0.4D$ into account (corresponding to the difference in length of the shear

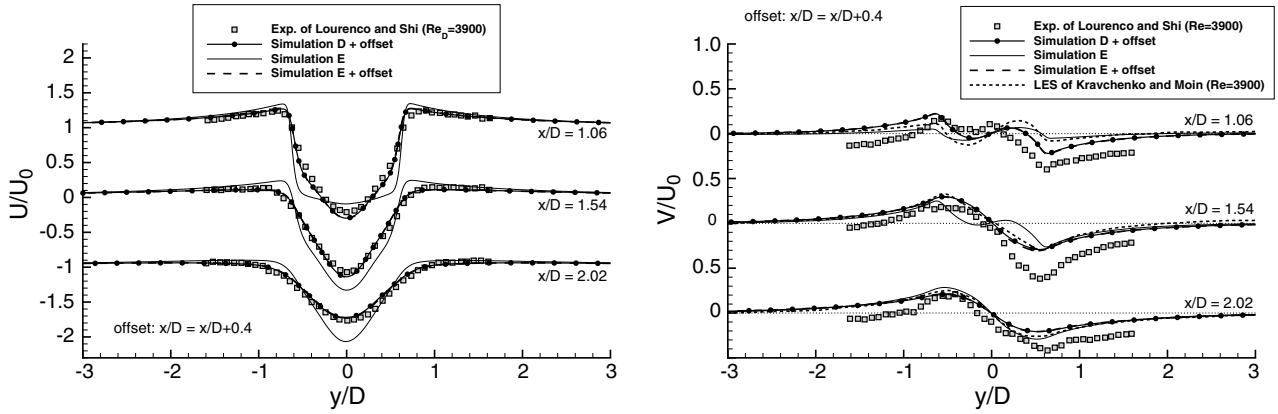


**Fig. 7.** Comparison of mean velocity profiles in the very near wake to the experiments of Lourenco and Shih (1993), left: mean $u$-velocity, right: mean $v$-velocity. The mean $v$-velocity is also compared to the LES results of Kravchenko and Moin (data taken from Kravchenko and Moin, 2000).

layer in the DNS compared to experiment) results in a very good agreement of the mean $u$-velocity profiles of both Simulations D and E with experiment. The difference between Simulations D and E – both with offset – can be seen to be very small. Hence, the effect of the largest spanwise mode, which is only resolved in Simulation E – on the mean $u$-velocity profile is only marginal.

Fig. 7 (right) shows a comparison of the mean $v$-velocity profiles with the experimental results of Lourenco and Shih at $x/D = 1.06, 1.54, 2.02$. While both DNS are in very good agreement with one another – again indicating the small influence of the presence of the largest spanwise mode – for all profiles, the comparison with the experimental data is found to be less favourable. This, however, might be due to the experimental data since Kravchenko and Moin (2000) observed a similar discrepancy in the mean $v$-velocity profiles when comparing them to their LES results at $Re = 3900$. As can be seen in the figure, the LES and DNS results are not identical, but are in better agreement with one another than with experiment. The difference between LES and DNS – which is most pronounced at $x/D = 1.06$ and virtually negligible at $x/D = 2.02$ – is again attributed to the different Reynolds numbers employed in the two sets of simulations.

The profiles of the mean $u$-velocity displayed in Fig. 8 illustrate that – also downstream of $x/D = 6$ – a very good agreement between the experimental data of Lourenco and Shih (1993) and Simulations D and E (using an offset of $0.4D$ in the streamwise direction) is obtained.

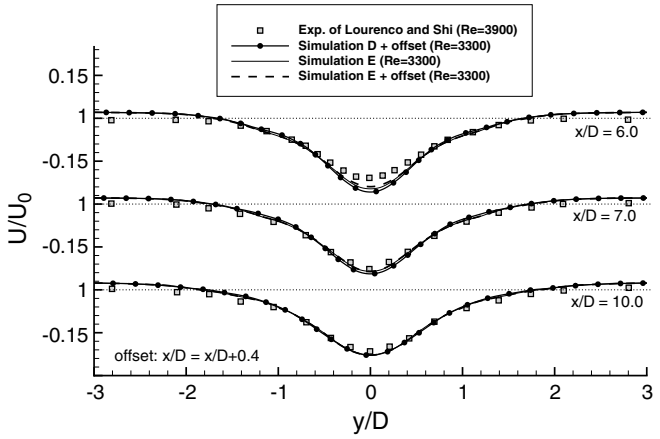


**Fig. 8.** Comparison of mean $u$-velocity profiles in the wake to the experiments of Lourenco and Shih (1993).

Fig. 9, finally, shows that also the streamwise normal stress and the shear stress from Simulations D and E (with offset) are in good agreement with experiment. Only at $x/D = 7$ and $x/D = 10$, the DNS predicts slightly smaller values for $\overline{u'u'}$ in the region around $y/D = 0$, though the magnitude of the two maximums at $y/D \approx \pm 0.7$ is well predicted.

In general, Simulations D and E show very similar results. This indicates that the influence of the spanwise size ($4D$ in Simulation D vs. $8D$ in Simulation E) on the time-averaged statistics is relatively small. To further investigate the importance of the largest spanwise mode in Simulation E, at $x/D = 2, 4, 6, 8$ and $y/D = 0$, the spanwise autocorrelation of the $u$-velocity,

$$\rho[\tilde{u}(x,0,z_0),\tilde{u}(x,0,z_0+z)] = \frac{\mathrm{cov}[\tilde{u}(x,0,z_0),\tilde{u}(x,0,z_0+z)]}{\{\mathrm{var}[\tilde{u}(x,0,z_0)]\mathrm{var}[\tilde{u}(x,0,z_0+z)]\}^{1/2}},$$

where $z_0 = 4D$, is determined as a function of $z$ from a series of snapshots. To calculate the autocorrelation, from each snapshot the spanwise-averaged value $u_S$ of $u$ is subtracted, i.e., $\tilde{u} = u - u_S$. Subsequently, the autocorrelation of $\tilde{u}$ is determined in the spanwise direction as a function of space. This autocorrelation function is shown in Fig. 10 in various streamwise locations along the line $y/D = 0$. It can be seen that the autocorrelation does not converge to zero for $z/D \to 4D$. This indicates that even in Simulation E, the spanwise size of $8D$ might not be large enough to accommodate all spanwise structures. Hence, to correctly reproduce the physics in numerical simulations of flow around a cylinder in the lower subcritical range in all detail, the spanwise size should be even larger than $8D$, which is currently beyond the limits of the available computational resources.

### 3.3. Phase-averaged statistics

In this section the focus will be on the phase-averaged statistics gathered in Simulation E. Though part of the variation in the phase-averaged statistics is accounted for by large scale differences in size of the shed vortices, the statistics do provide valuable insight in, for instance, the dynamics of the vortex shedding and the exact location of production of turbulence kinetic energy.

Fig. 11 shows contours of the phase-averaged spanwise vorticity $\langle\omega_z\rangle_\phi$ at four different phases $\phi = 0, \frac{1}{4}, \frac{2}{4}, \frac{3}{4}$. At each phase two-dimensional shear layers can clearly be identified at $y/D \approx \pm\frac{1}{2}$, immediately behind the cylinder. The series of contours illustrate one period of vortex shedding. At $\phi = 0$, the downstream part of the lower shear layer is about to shed, while the upper shear layer (identified by dark contours of negative spanwise vorticity) is about to roll up. At $\phi = \frac{1}{4}$, the lower shear layer has shed a vortex and started to roll-up again while the upper shear layer extended

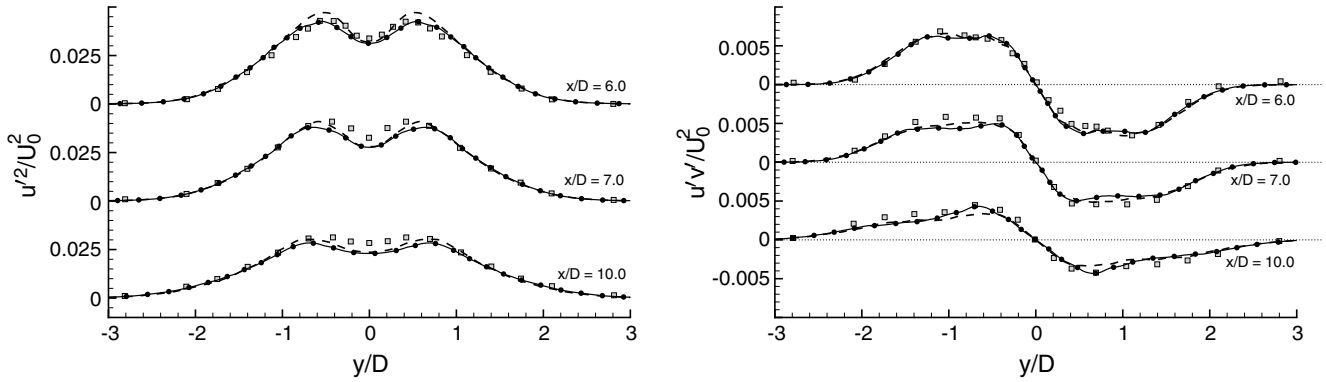


**Fig. 9.** Comparison of turbulence statistics in the wake to the experiments of Lourenco and Shih (1993), left: $\overline{uu}/U_0^2$, right: $\overline{uv}/U_0^2$ (see Fig. 8 for the legend).

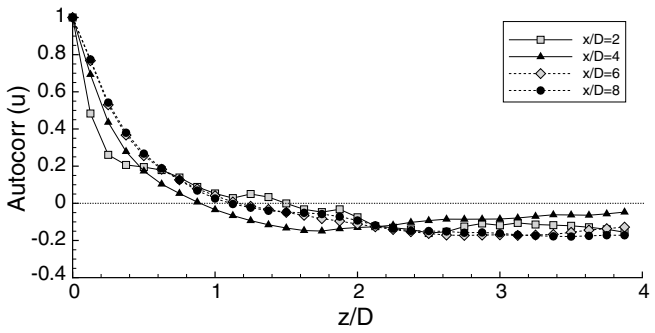


**Fig. 10.** Simulation E: Spanwise autocorrelation of $u$ at various streamwise locations along $y/D = 0$.

farther downstream. The snapshot at $\phi = \frac{2}{4}$ shows that the downstream part of the upper shear layer is about to be shed. while the lower shear layer is rolling up. At $\phi = \frac{3}{4}$, finally, a very similar situation is obtained as the one observed at $\phi = \frac{1}{4}$ but with the roles of upper and lower shear layers interchanged.

Note that most of the contours downstream of $x/D = 1$, as illustrated in Figs. 11–14, are slightly irregular. The reason for this is that – because of limitations in the computational resources – the phase-averaging procedure was only carried out during 10 vortex shedding cycles.

Fig. 12 shows contours of the phase-averaged turbulence kinetic energy $\langle k \rangle_\phi$ at the same phases as the ones used in Fig. 11. The series of plots clearly show the formation of a vortex street of which the location is identified by increased levels of turbulence kinetic energy. By comparing the contours of $\langle \omega_z \rangle_\phi$ and $\langle k \rangle_\phi$ at $\phi = \frac{2}{4}$, a local peak in $\langle k \rangle$ can be seen to almost coincide with the centre of the rolled up part of the lower shear layer. In Fig. 13 this event is identified by a circle labeled "B", which provides a zoomed view of the corresponding contours at $\phi = \frac{2}{4}$ as displayed in Figs. 11 and 12. The circle labeled "A" identifies a similar situation for the upper shear layer. Here too, the peak in $\langle k \rangle$ can be seen to be located inside the rolled up part of the shear layer.

Fig. 14 shows contours of the phase-averaged shear stress $\langle u'v' \rangle_\phi$ for $\phi = 0, \frac{1}{4}, \frac{2}{4}, \frac{3}{4}$. This figure illustrates the presence of shear stress generated at those locations where the two shear layers behind the cylinder disintegrate. This can be seen by comparing

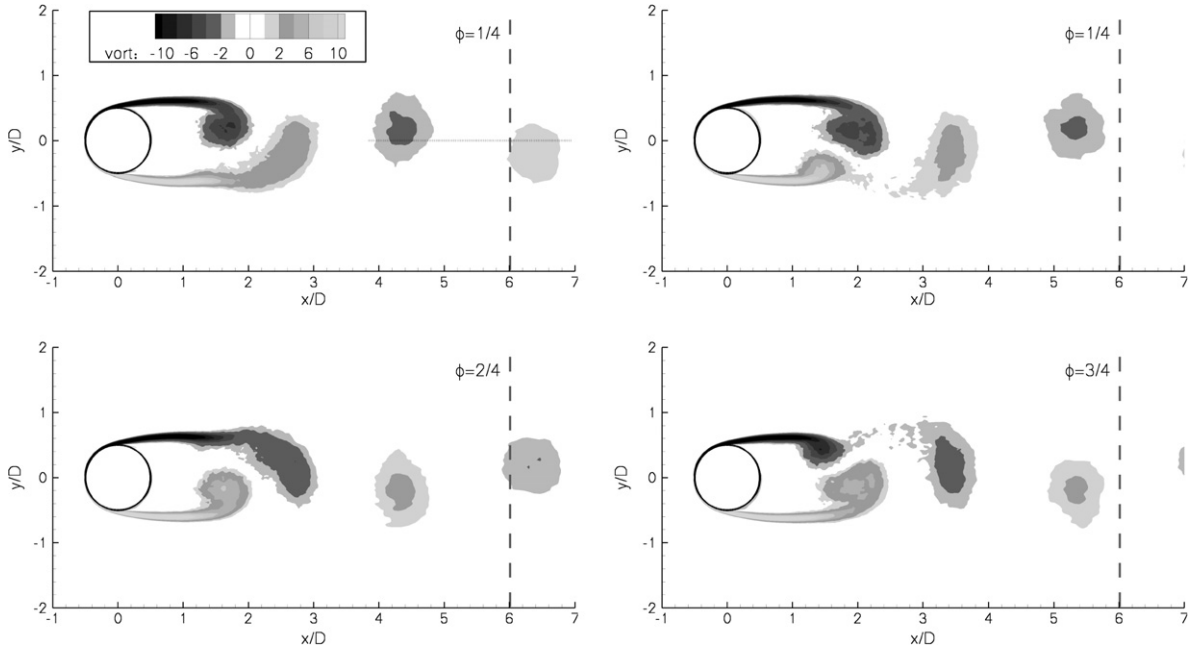


**Fig. 11.** Contours of the phase-averaged spanwise vorticity $\langle \omega_z \rangle_\phi$ at $\phi = 0, 1/4, 2/4, 3/4$, the horizontal dotted line in the upper left pane identifies the location where the phase-averaged streamwise velocity shown in Fig. 18 was extracted, while the vertical dashed lines identify the location of the plane at which wake data was extracted.

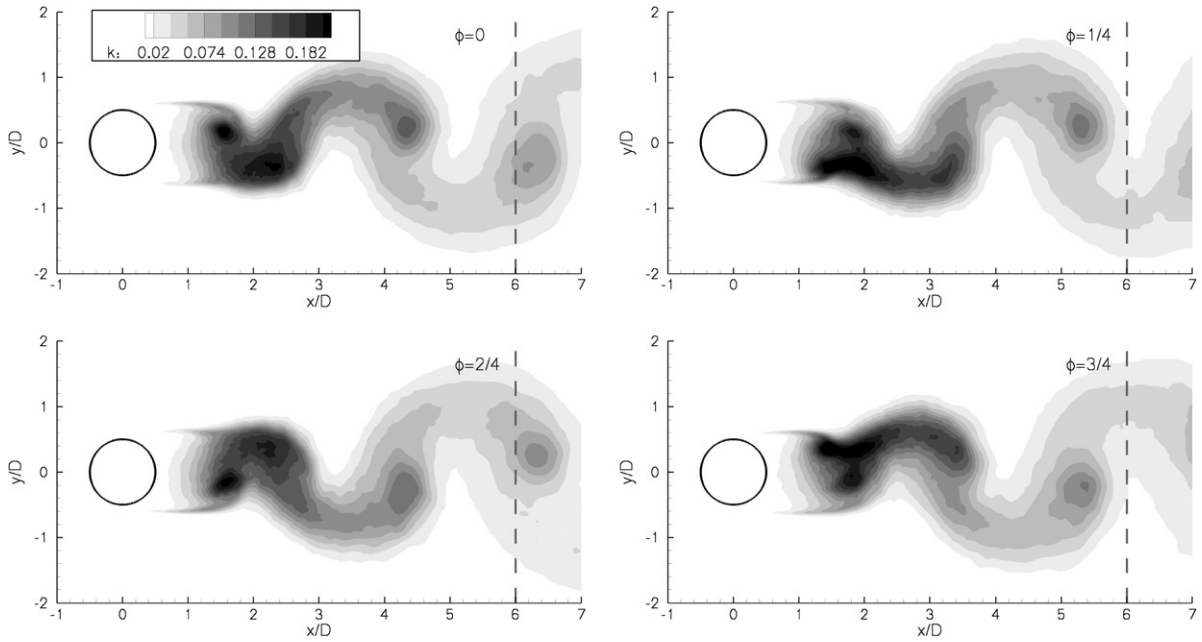


**Fig. 12.** Contours of the phase-averaged turbulence kinetic energy $\langle k \rangle_\phi$ at $\phi = 0, 1/4, 2/4, 3/4$, the vertical dashed lines identify the location of the plane at which wake data was extracted.

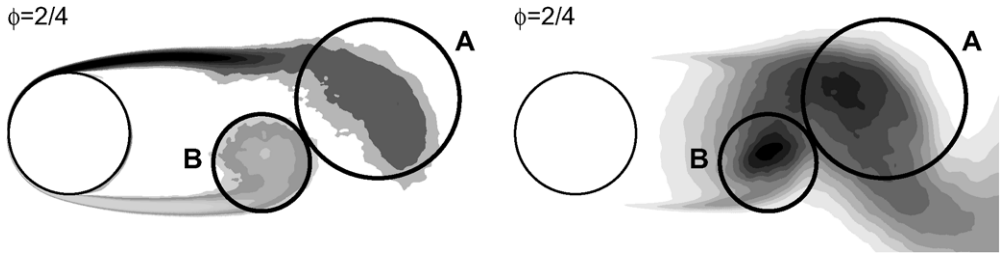


**Fig. 13.** Close-up of the phase-averaged spanwise vorticity $\langle \omega_z \rangle_\phi$ (left) and turbulence kinetic energy $\langle k \rangle_\phi$ (right) at $\phi = 2/4$ in the very near wake of the cylinder.

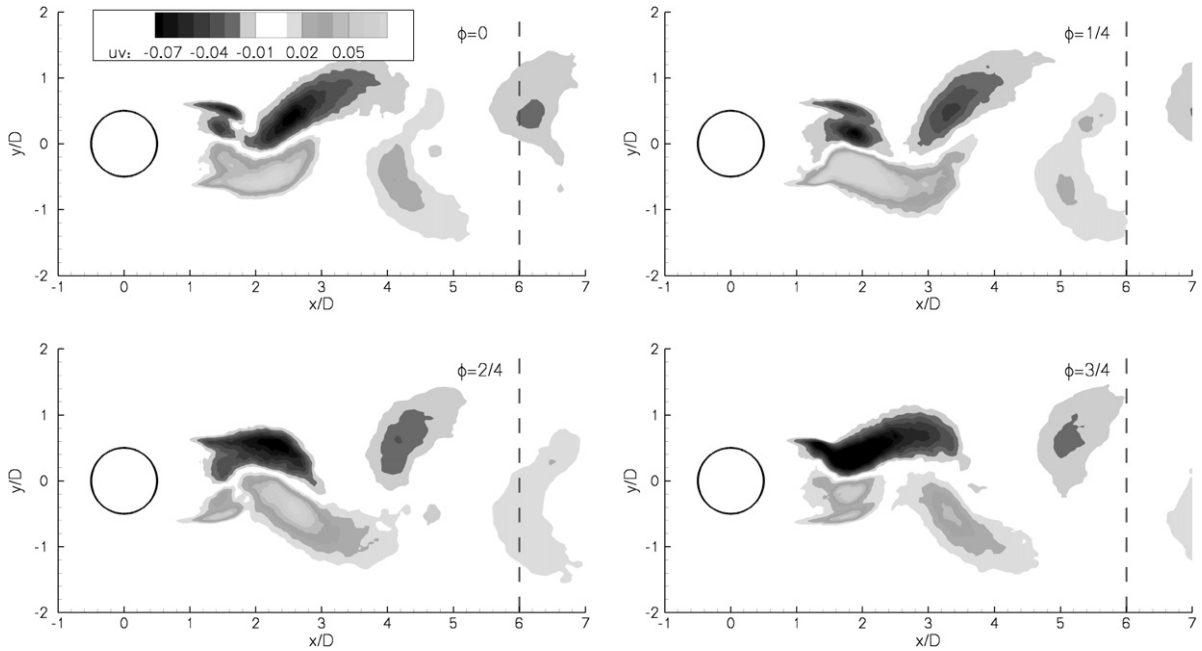


**Fig. 14.** Contours of the phase-averaged shear stress $\langle uv \rangle_\phi$ at $\phi = 0, 1/4, 2/4, 3/4$, the vertical dashed lines identify the location of the plane at which wake data was extracted.

Fig. 14 with Fig. 11 showing a correlation between the destruction of positive spanwise vorticity and positive shear stress on the one hand and the destruction of negative spanwise vorticity and negative shear stress on the other hand. Below, this will be analyzed in more detail.

Consider the phase-averaged production, $P_{12}$, of shear stress $\langle u'v' \rangle$ for a flow that is homogenous in the spanwise direction. For such a flow $\langle u'w' \rangle = \langle v'w' \rangle = 0$, $\langle u'v' \rangle = \langle v'u' \rangle$ and, because of continuity, $\frac{\partial \langle u \rangle}{\partial x} = -\frac{\partial \langle v \rangle}{\partial y}$ (since $\frac{\partial \langle w \rangle}{\partial z} = 0$), such that

$$P_{12} = -\left[\langle u_1' u_k' \rangle \frac{\partial \langle u_2 \rangle}{\partial x_k} + \langle u_2' u_k' \rangle \frac{\partial \langle u_1 \rangle}{\partial x_k}\right] = -\left[\langle u'u' \rangle \frac{\partial \langle v \rangle}{\partial x} + \langle v'v' \rangle \frac{\partial \langle u \rangle}{\partial y}\right],$$

where $u_1 = u$, $u_2 = v$, $u_3 = w$, $x_1 = x$, $x_2 = y$ and $x_3 = z$. As can be seen in Fig. 15, at the locations where the upper and lower shear layer disintegrate – as in Fig. 13 identified by the two circles labeled "A" and "B", respectively – the contribution of $\langle uu \rangle_\phi$ to $\langle k \rangle_\phi$ is smaller than the contribution of $\langle vv \rangle_\phi$. Hence, the most important term that contributes to $P_{12}$ – in the case of a horizontal shear layer – is $-\langle v'v' \rangle \frac{\partial \langle u \rangle}{\partial y}$, while the most important term contributing to the phase-averaged vorticity, $\langle \omega_z \rangle$, is $-\frac{\partial \langle u \rangle}{\partial y}$. Thus one expects to see production of shear stress at locations inside the horizontal shear layer where there is production of $\langle v'v' \rangle$ and the sign of the produced shear stress will be the same as the sign of the spanwise vorticity it feeds from. From this one can conclude that for this problem the production of shear stress in the horizontal shear layer is directly related to the destruction of vorticity, or, equivalently, mean shear.

Fig. 16, finally, shows the location of separation, $\langle \alpha \rangle_\phi$ as a function of phase. The location is given in degrees, where $\langle \alpha \rangle_\phi = 0$ corresponds to the stagnation line at the front of the cylinder. One can clearly see that the location of separation moves alternately upstream and downstream. Compared to the time-averaged location of separation, $\alpha = 87.4°$, the amplitude of the phase-averaged signal can be seen to be approximately 0.9°.

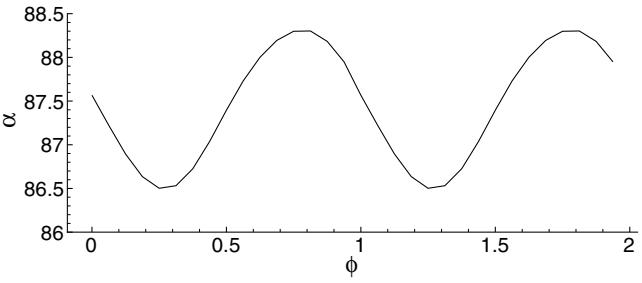


**Fig. 16.** Simulation E: Location of separation as a function of phase.

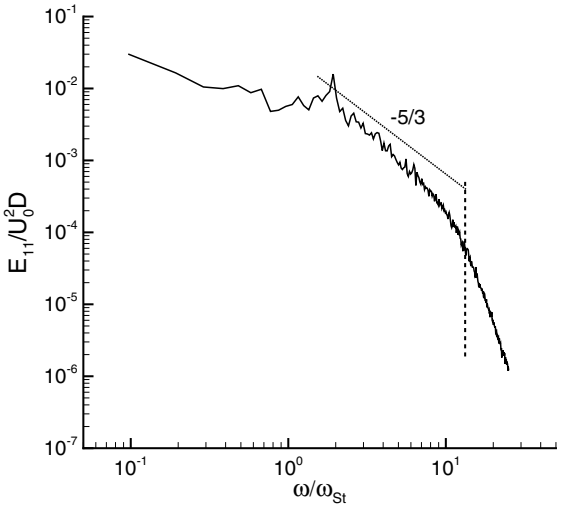


**Fig. 17.** Simulation E: Energy spectrum at $x/D = 6$ as a function of the non-dimensional frequency.

### 3.4. Analyses of flow field at x/D = 6

To conclude the results section, the snapshots of the flow field gathered in Simulation E at $x/D = 6$ – that will be used in future simulations of flow and heat transfer in a turbine cascade – are analyzed in more detail. The integral length-scale, $\Lambda$, of the $u$ fluctuations in the spanwise direction at the axis of the wake as determined by integrating the autocorrelation in Fig. 10 over $z$ (only for the part where $\rho$ is positive) is $\Lambda = 0.357D$. The energy spectrum at $x/D = 6, y/D = 0$, shown in Fig. 17, is produced using snapshots of the flow field gathered during ten vortex-shedding cycles. To obtain a relatively smooth result, the time spectra – calculated at various spanwise locations – were averaged. The angular frequency $\omega = 2\pi f$ was made non-dimensional using $\omega_{St} = 2\pi St$, where $St$ is the Strouhal number. The figure shows the presence of an inertial range and is very similar to the time-spectra obtained by Kravchenko and Moin (2000) at $Re = 3900$ and $x/D = 7$. For instance, the frequency range of the inertial range is virtually identical.

The local peak in the spectrum at $\omega/\omega_{St} = 2$ exactly corresponds to twice the shedding frequency of the vortices. This is explained by the fact that in every shedding cycle two vortices of opposite sign are shed from the upper and lower side, respectively, of the cylinder. The effect of these vortices – identified by the phase-averaged vorticity shown in Fig. 11 – on the phase-averaged streamwise velocity, $\langle u \rangle_\phi$, extracted at $\phi = 0$ along a finite line at $y/D = 0$, is illustrated in Fig. 18. The location of the line is identified by the dotted horizontal line in Fig. 11 (upper left pane), which can be seen to intersect with two vortices. While the centre of the left (clockwise rotating) vortex is located above the line, the centre of the right (counterclockwise rotating) vortex is located below the line. Because of the vertical offsets of the two vortices, they both induce a local minimum in the $\langle u \rangle_\phi$ profile. In between each of the vortices, $\langle u \rangle_\phi$ reaches a local maximum. Hence, the two vortices induce a variation in the phase-averaged $u$-velocity that very much resembles two periods of a harmonic oscillation. Using the fact that

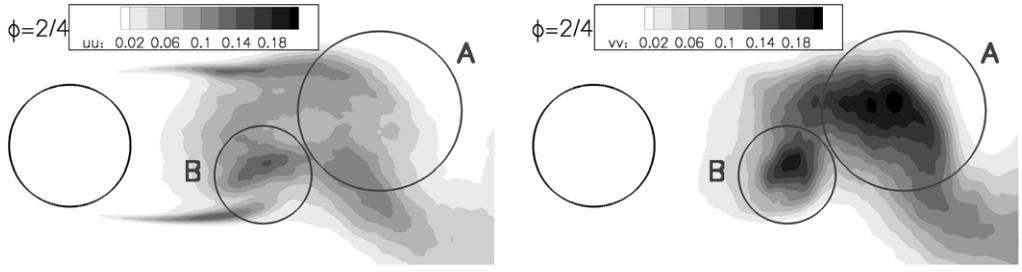


**Fig. 15.** Close-up of the phase-averaged normal stresses $\langle uu \rangle_\phi$ (left) and $\langle vv \rangle_\phi$ (right) at $\phi = 2/4$ in the very near wake of the cylinder.

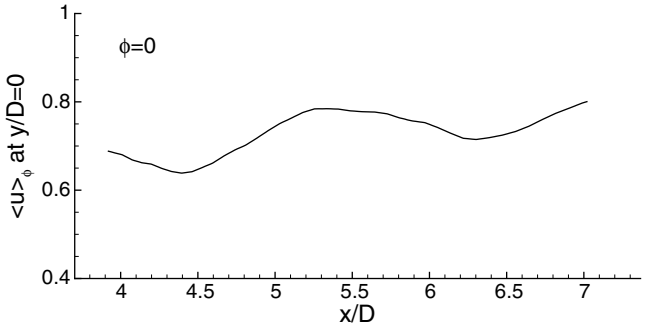


**Fig. 18.** Simulation E: Phase-averaged $u$-velocity, $\langle u\rangle_\phi$, at $\phi = 0$ along part of the axis of the computational domain. The location where $\langle u\rangle_\phi$ has been extracted is identified by the horizontal dotted line in Fig. 11.

the vortices in the wake are passively convected downstream by the mean flow $U$, we may interchange the $x$-coordinate by time (or equivalent phase) and, hence, conclude that the phase-averaged $u$-velocity at $x/D = 6$ will exhibit two minima in the interval $0 \leqslant \phi < 1$, which explains the peak at $\omega/\omega_{St} = 2$.

As can be seen in the Figs. 11, 12 and 14 – where the location of the extracted data is identified by a dashed, vertical line – at $x/D = 6$, the remains of the vortices shed from the upper and lower side of the cylinder, respectively, are clearly identifiable. The sequences of phase-averaged data displayed in these figures show the presence of unsteady large scale movement over the complete width of the wake. These coherent structures are typical for the near wake of a cylinder. In further simulations we intent to investigate their effect on the increase in heat transfer as they impinge on a laminar, accelerating boundary layer.

In Fig. 19, finally, a series of snapshots of instantaneous velocity vectors in the $(y,z)$ plane of the computational domain at $x/D = 6$, covering approximately one period of vortex shedding, is shown. The snapshots at $t = 30.00D/U_0$ and $t = 32.40D/U_0$ clearly show the presence of secondary recirculation areas with a diameter of approximately $1D$, a bit more than twice the integral length-scale $\Lambda$ of the $u$ velocity fluctuations in the spanwise direction. These two snapshots also illustrate the vertical meandering of the wake as the centre line of the wake moves from $y/D \approx 0.5$ at $t = 30.00D/U_0$ to $y/D \approx -0.5$ at $t = 32.40D/U_0$. This large vertical meandering motion is also confirmed by the vector fields displayed in the snapshots taken at $t = 31.20D/U_0$ and $t = 33.60D/U_0$ that show a large scale movement of the wake in the negative and positive $y$-direction, respectively.

## 4. Discussion and conclusions

To obtain high-quality realistic wake data for use in further simulations of flow and heat transfer in a turbine cascade with incoming wakes, a series of DNS of incompressible flow around a circular cylinder has been performed for a Reynolds number of $Re = 3300$ – which is in the lower subcritical regime. The flow is characterized by the presence of two free-shear layers immediately behind the cylinder. To obtain a proper representation of the flow physics in

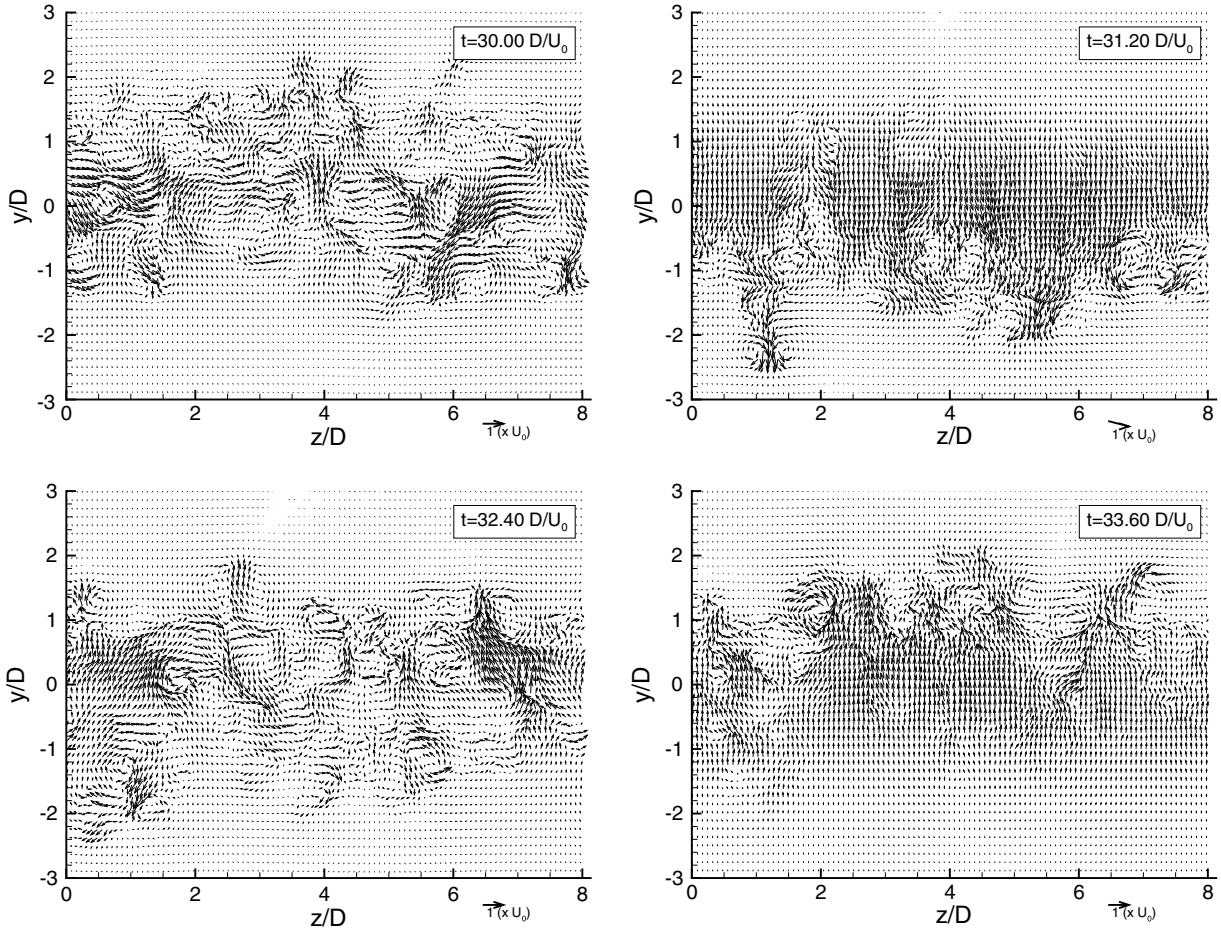


**Fig. 19.** Simulation E: Snapshots at $t = 30.00, 31.20, 32.40, 33.60D/U_0$, showing instantaneous $(w,v)$-velocity vectors in the plane at $x/D = 6$, identified by the vertical dashed lines in Figs. 11, 12, and 14. In the $y$-direction every 5th vector is shown, while in the $z$-direction every 10th vector is shown.

the very near wake, it was found to be very important that the two shear layers are well-resolved.

The non-dimensional shedding frequency represented by the Strouhal number $St$ was found to be rather insensitive to the actual resolution of the flow. Values between $St = 0.214$ and $St = 0.221$ were obtained without any clear convergence towards a unique value. Hence, it is very likely that the accuracy of this value depends more on the number of shedding cycles employed to estimate this average than on the actual grid used in the DNS. With an increasingly fine mesh, the time-averaged location of separation, however, did show a clear convergence to a value of approximately $\alpha = 87.4°$.

Apart from a slight offset in the streamwise direction of $x/D = 0.4$, the well-resolved DNS results were found to compare well with the experimental results of Lourenco and Shih (1993). The offset was accounted for by (1) the usage of a Reynolds number in the DNS of $Re = 3300$ – compared to $Re = 3900$ in the experiment – and (2) by the likely presence of background noise in the experiment that resulted in a reduction in size of the separation bubble behind the cylinder (see also Kravchenko and Moin, 2000).

One of the main aims of the present simulations was to address the effect of the spanwise size of the computational domain on the turbulence statistics in the near wake. To this end, two similarly resolved DNS were performed, the first one with a spanwise size of $l_z = 4D$ and the second one with a spanwise size of $l_z = 8D$. A direct comparison of the turbulence statistics obtained in these two simulations showed very similar – though not completely identical – results. To investigate the importance of the largest spanwise mode in more detail, the spanwise autocorrelation of the streamwise velocity at $x/D = 2, 4, 6, 8$ was determined for Simulation E, showing that – even in the Simulation E – the width of the computational domain ($l_z = 8D$) – was probably not entirely sufficient to accommodate the largest spanwise scales of motion. However, it has to be stressed that this has very little effect on the calculation of the turbulence statistics so that a good agreement between DNS and experiments was achieved.

The phase-averaged statistics have shown that turbulence kinetic energy contours are a very useful tool for identifying the location of the vortex street. To elucidate the actual formation of this vortex street immediately behind the cylinder, the study of the phase-averaged spanwise vorticity was found to be very helpful. The production of turbulence kinetic energy was observed to be mainly concentrated at those locations where the shear layers immediately behind the cylinder first roll-up. Further analysis has shown that there is a correlation between the production of phase-averaged shear stress $\langle uv\prime v\prime\rangle$ and the generation of turbulence – or to be more precise the generation of $\langle v\prime v\prime\rangle$ – in a predominantly horizontal shear layer where $\langle \omega_z \rangle \approx -\frac{\partial \langle u \rangle}{\partial y}$. In this case, the shear is of the same sign as the vorticity, which is also observed in the DNS.

Owing to the alternate shedding of vortices from the shear layers originating from the upper and lower side of the cylinder, respectively, the phase-averaged location of separation, was found to undergo a slight oscillation, with an amplitude of approximately 0.9°, around its time-averaged value.

At the plane $x/D = 6$ – where a series of snapshots of the flow field was gathered – the wake was found to consist of large, meandering coherent structures. These coherent structures are typical for a turbulent near wake. The absence of such structures in the artificial wake data – corresponding to a turbulent far wake – used in the DNS of flow and heat transfer around a turbine blade reported in Wissink and Rodi (2006) may explain the failure of the DNS in correctly reproducing the significant, wake-induced increase in laminar heat transfer as observed in the experiments of Liu and Rodi (1994a,b). The energy spectrum at $y/D = 0$ clearly shows the presence of an inertial range at the axis of the turbulent wake at $x/D = 6$. The peak observed at twice the time-averaged shedding frequency can be explained by studying the effect of the vortices from the vortex street on the local streamwise velocity, $u$. Since each individual vortex gives rise to a minimum in the $u$-velocity, in each vortex shedding period two minima are obtained which results in a frequency doubling and explains the location of the peak in the energy spectrum at $2\omega/\omega_{st}$.

## Acknowledgements

The authors would like to thank the German Research Foundation (DFG) for funding this research and the Steering Committee of the High Performance Computing Centre (HLRS) in Stuttgart for granting computing time on the NEC SX8.

## References

Beaudan, P., Moin, P., 1994, Numerical experiments on the flow past a circular cylinder at sub-critical Reynolds number. In Report No. TF62, Thermosciences Division, Department of Mechanical Engineering, Stanford University, pp. 1–44.
Breuer, M., 1998. Large eddy simulations of the subcritical flow past a circular cylinder: numerical and modelling aspects. Int. J. Numer. Meth. Fluids 28, 1281–1302.
Breuer, M., Rodi, W., 1996. Large eddy simulation for complex turbulent flow of practical interest. In: Hirschel, E.H. (Ed.), Notes in Numerical Fluid Mechanics, vol. 52. Vieweg Verlag, Braunschweig.
Dong, S., Karniadakis, G.E., Ekmekci, A., Rockwell, D., 2006. A combined direct numerical simulation-particle image velocimetry study of the turbulent near wake. J. Fluid Mech. 569, 185–207.
Fröhlich, J., Rodi, W., Kessler, Ph., Parpais, S., Bertoglio, J.P., Laurence, D., 1998. Large eddy simulation of flow around circular cylinders on structured and unstructured grids. In: Hirschel, E.H. (Ed.), Notes in Numerical Fluid Mechanics, vol. 66. Vieweg Verlag, Braunschweig.
Kravchenko, A.G., Moin, P., 2000. Numerical studies of flow around a circular cylinder at $Re_D = 3900$. Phys. Fluids 12, 403–417.
Liu, X., Rodi, W., 1994a. Surface pressure and heat transfer measurements in a turbine cascade with unsteady oncoming wakes. Exp. Fluids 17, 171–178.
Liu, X., Rodi, W., 1994b. Velocity measurements of wake-induced unsteady flow in a linear turbine cascade. Exp. Fluids 17, 45–58.
Lourenco, L.M., Shih, C., 1993, Characteristics of the plane turbulent near wake of a circular cylinder, a particle image velocimetry study, Published in Beaudan and Moin (1994), data taken from Kravchenko and Moin (2000).
Ma, X., Karamonos, G.-S., Karniadakis, G.E., 2000. Dynamics of low-dimensionality of a turbulent near wake. J. Fluid Mech. 410, 29–65.
Mittal, R., Moin, P., 1997. Suitability of upwind-biased finite-difference schemes for large eddy simulations of turbulent flows. AIAA J. 35, 1415–1417.
Monkewitz, P.A., 1988. The absolute and convective nature of instability in two-dimensional wakes at low Reynolds numbers. Phys. Fluids 31, 999–1006.
Norberg, C., 1994. An experimental investigation of flow around a circular cylinder: influence of aspect ratio. J. Fluid Mech. 258, 287–316.
Norberg, C., 2003. Fluctuating lift on a circular cylinder: review and new measurements. J. Fluids Struct. 17, 57–96.
Ong, J., Wallace, L., 1996. The velocity field of the turbulent very near wake of a circular cylinder. Exp. Fluids 20, 411–453.
Rhie, C.M., Chow, W.L., 1983. Numerical study of the turbulent flow pas an airfoil with trailing edge separation. AIAA J. 21, 1525–1532.
Stone, H.L., 1968. Iterative solutions of implicit approximations of multidimensional partial differential equations. SIAM J. Numer. Anal. 5, 87–113.
Thompson, M., Hourigan, M., Sheridan, J., 1996. Three dimensional instabilities in the wake of a circular cylinder. Exp. Therm. Fluid Sci. 12, 190–196.
Williamson, C.H.K., 1996a. Three dimensional wake transition. J. Fluid Mech. 328, 345–407.
Williamson, C.H.K., 1996b. Vortex dynamics in the cylinder wake. Ann. Rev. Fluid Mech. 28, 477–539.
Wissink, J.G., Rodi, W., 2006. Direct numerical simulation of flow and heat transfer in a turbine cascade with incoming wakes. J. Fluid Mech. 569, 209–247.